Materials Advances

ROYAL SOCIETY OF CHEMISTRY

PAPER

View Article Online
View Journal | View Issue

Check for updates

Cite this: *Mater. Adv.*, 2026, 7, 5768

Clitoria ternatea-mediated ZnO nanoparticles for enzyme-free photoelectrochemical cholesterol detection

Sushmitha S,[a] Lavanya Rao,[a] Mahesha P. Nayak,[a] Shreeganesh Subraya Hegde[b] and Badekai Ramachandra Bhat*[a]

A reliable and enzyme-free investigation of cholesterol is essential for the timely detection and diagnosis of cardiac disorders. Herein, we report the synthesis of zinc oxide (ZnO) nanoparticles *via* a wet chemical method, incorporating the *Clitoria ternatea* (CT) flower extract as a sustainable phytochemical-mediated approach, where the CT-ZnO/nickel foam (NF) acts as an active material for a novel photoelectrochemical (PEC) biosensor. The study highlights the significant improvement in sensitivity for cholesterol sensing in light mode, with a value of 956 μA mM^{-1} cm^{-2}, which is twice as high as without light (492.5 μA mM^{-1} cm^{-2}). Improvements in the limit of detection (LOD) (35 μM and 28 μM, respectively) and limit of quantification (LOQ) (110 μM and 95 μM, respectively) without and with light were observed in 0.1 M KOH with a response time of 2 s. The above findings reveal a linear detection range of 0 μM–2 mM. The CT-ZnO/NF PEC biosensor demonstrated exceptional cyclic stability, retaining 98.8% of its efficiency for 90 days. In addition, the reliable performance of CT-ZnO/NF demonstrated remarkable sensing abilities of 88–93% when testing on human serum samples. This research illustrates the dual electrochemical and photoelectrochemical properties of novel green-engineered ZnO, providing an effective and sustainable platform for non-enzymatic cholesterol monitoring in healthcare diagnostics.

Received 12th January 2026,
Accepted 20th April 2026

DOI: 10.1039/d6ma00056h

rsc.li/materials-advances

Open Access Article. Published on 19 May 2026. Downloaded on 6/21/2026 8:54:41 PM.
This article is licensed under a Creative Commons Attribution-NonCommercial 3.0 Unported Licence.

1. Introduction

Cholesterol is an essential biomolecule that facilitates many biochemical pathways, including maintaining membrane integrity, and is involved in synthesizing hormones.[1,2] Despite this, hypercholesterolemia, where the cholesterol levels are more than 6.21 mM (240 mg dL^{-1}) in the bloodstream, is closely linked to cardiac disease and stroke.[3] As a consequence, tracking the levels of cholesterol in biological fluids precisely and quickly has grown into a crucial aspect for both clinical and preventative healthcare.[4–6]

Conventional enzymatic cholesterol biosensors offer outstanding specificity and sensitivity, primarily built around cholesterol oxidase or cholesterol esterase.[7] However, fundamental limitations, including enzyme instability, expensive production, sensitivity to pH and temperature, and intricate immobilisation procedures, preclude their widespread adoption.[8,9] Given these shortcomings, there is a significant need for the design and development of non-enzymatic electrochemical sensors with improved durability, reduced manufacturing costs, and reliable long-term performance.[10–13] Photoelectrochemistry has grown into a key field in photovoltaics and biosensing since the groundbreaking discovery of the photoelectric effect by Becquerel in 1839.[14,15] It analyses the way light interacts with photoactive materials, where photon absorption promotes the emission of electrons and holes, separates charges, and then performs redox processes at the electrode–electrolyte interface, resulting in a detectable photocurrent.[16–19] By minimising disturbances and taking advantage of light-driven signal amplification, PEC biosensors frequently surpass conventional electrochemical techniques in the fast, economical, and highly sensitive analyte detection process.[18,20–22]

Meanwhile, ''green'' nanotechnology has evolved into an economically feasible approach that incorporates sustainable chemistry principles for the synthesis of nanostructures.[23] Employing phytochemicals derived from flowers as reducing, capping, and stabilising agents has been identified as a sustainable and profitable strategy.[24,25] Apart from aiding in the nucleation and development of nanoparticles, phytochemical-rich extracts can alter their structural and electrical attributes

[a] *Department of Chemistry, Catalysis and Materials Chemistry Laboratory, National Institute of Technology, Surathkal, D.K., Karnataka, 575 025, India. E-mail: ram@nitk.edu.in*
[b] *Department of Chemistry, School of Engineering, Dayananda Sagar University, Harohalli, Bengaluru, Karnataka, 562112, India*

© 2026 The Author(s). Published by the Royal Society of Chemistry

Open Access Article. Published on 19 May 2026. Downloaded on 6/21/2026 8:54:41 PM. This article is licensed under a Creative Commons Attribution-NonCommercial 3.0 Unported Licence.

via surface functionalisation.[26–28] *Clitoria ternatea* (CT) or butterfly pea is a medicinally valuable species known to possess an enormous volume of anthocyanins, flavonoids, and polyphenols.[29–31] These bioactive components are excellent candidates for influencing the morphology and electrochemical activity of nanoparticles owing to their powerful antioxidant and metal-chelating capabilities.[32,33] Additionally, these materials operate as stabilizing and functionalizing agents, thereby enhancing photoinduced activity and facilitating improved charge transfer efficiency.[34]

There have been a handful of literature reports on PEC cholesterol biosensors, and their potential remains largely unexplored. By employing iron-modified $CuBiO_4$ (CBFO) as the photocathode and ZnO/C-modified FTO as the photoanode, a self-powered PEC sensor for cholesterol detection was designed. For better selectivity, molecularly imprinted polymers (MIPs) were electrodeposited. The sensor displayed good recoveries (98.6–107%) in milk samples and a broad linear range (1–1000 nmol L^{-1}) with a detection limit of 0.26 nmol L^{-1}, confirming its potential for real-world uses.[35] A TiO_2 inverse opal/$CH_3NH_3PbBr_3$ quantum dot heterojunction on ITO was utilised to produce a PEC cholesterol sensor, which exhibited an enhanced photocurrent density of $\sim$40 μA cm^{-2}. The selectivity and stability were improved *via* encapsulation using molecularly imprinted polymers, with high recovery in blood samples, a low detection limit (2.51×10^{-10} mol L^{-1}), retention of 80% of the photocurrent in aqueous solution after 500 s, and storage stability for 20 days.[36] Ce-doped ZnO ($Ce_xZn_{1-x}O$) was obtained *via* a wet chemical process to serve as the key component in a PEC cholesterol biosensor. The sensor exhibited a linear range of 80 μM–2 mM, a sensitivity of 2.812 mA mM^{-1} cm^{-2} under light, and LODs of 17 μM (light) and 28 μM (dark). The utility of the sensor is demonstrated by its 97% stability over 60 days and reliable operation in human serum samples.[21] A comparison of the literature, based on the analysis of electrochemical performance with previously reported green-synthesized sensors, is presented in Table S1.

Although the field of PEC cholesterol sensors has evolved considerably, a number of published strategies lack ecologically feasible synthesis techniques. ZnO, a semiconductor material, has been selected for this study due to its excellent thermal and mechanical stability. In addition, ZnO exhibits remarkable photocatalytic properties and has been widely explored for applications in electronic devices and environmental remediation.[37] Our research aims to bridge this gap by developing a sustainable nanostructured metal oxide for PEC sensing that fuses sustainability with enhanced reliability and sensitivity.

This investigation has adopted a wet chemical technique to synthesise ZnO nanostructures, both with and without the incorporation of CT flower extract. The goal was to assess the efficiency of ZnO as a non-enzymatic platform for cholesterol sensing and to elucidate the ways that phytochemical modulation impacts the material's structural, morphological, and electrochemical characteristics. This study contributes to the growing body of research supporting sustainable and green techniques in the production of advanced sensors, while also highlighting the potential of CT-mediated ZnO nanostructures for biosensing applications.

2. Synthesis of ZnO and CT-ZnO

ZnO nanomaterials were synthesised by dissolving 1 M $Zn(NO_3)_2$ in 100 mL of Milli-Q water under continuous stirring at 60 °C until a transparent solution was obtained. For the synthesis of CT-ZnO, 10 mL of flower extract was introduced into the zinc nitrate solution. In both cases, 1.5 M NaOH solution was added dropwise until the pH of the mixture reached 14, leading to the formation of a white precipitate. The resulting suspension was stirred at 60 °C for an additional 2 hours, followed by continued stirring at room temperature for 12 hours. The precipitate was then collected *via* centrifugation, washed, and dried. Finally, the dried product was calcinated at 500 °C for 2 hours. The resulting samples were designated as ZnO and CT-ZnO (zinc oxide synthesised in the presence of flower extract), respectively.

3. Mechanistic pathway for the plant-mediated system

ZnO nanoparticle synthesis by CT-flower extract mainly depends on the phytochemicals present in the CT flower, which facilitate the reaction by acting as antioxidants and nontoxic substances.[25] Important phytochemicals such as anthocyanins,[38] terpenoids, flavonoids, cardiac glycosides, and alkaloids aid in the reduction of metal ions; their amount and composition significantly affect the size, form, and production of nanoparticles. The synthesis and stabilisation mechanism is additionally impacted by parameters such as pH, temperature, reaction time, and precursor concentration.[39] Three phases play a role in the mechanism, as described by Makarov *et al.*: (i) activation (nucleation and reduction of metal ions), (ii) growth (stability and controlled assembly), and (iii) termination (final structure formation).[40,41] To produce biocompatible metal oxide nanoparticles, the phytochemicals stabilise and encapsulate metal ions as described in Scheme 1.

4. Results and discussion

The material formation was confirmed by X-ray diffraction, with the diffraction pattern matching the characteristic peaks of the crystalline ZnO (JCPDS Card No. 089–0510), verifying the hexagonal wurtzite structure, as illustrated in Fig. 1(a). Each CT-ZnO peak strongly matched that of ZnO, indicating the presence of ZnO without additional impurity peaks, thereby indicating that the synthesised material was in its purest form. The average crystallite sizes of the synthesised materials were calculated using the Debye–Scherrer equation and were 40 nm and 41 nm for ZnO and CT-ZnO, respectively. Fig. S1(a) shows a peak shift toward lower 2θ angles for ZnO, indicating the presence of phytochemicals from the flower extract on the

Open Access Article. Published on 19 May 2026. Downloaded on 6/21/2026 8:54:41 PM.
This article is licensed under a Creative Commons Attribution-NonCommercial 3.0 Unported Licence.

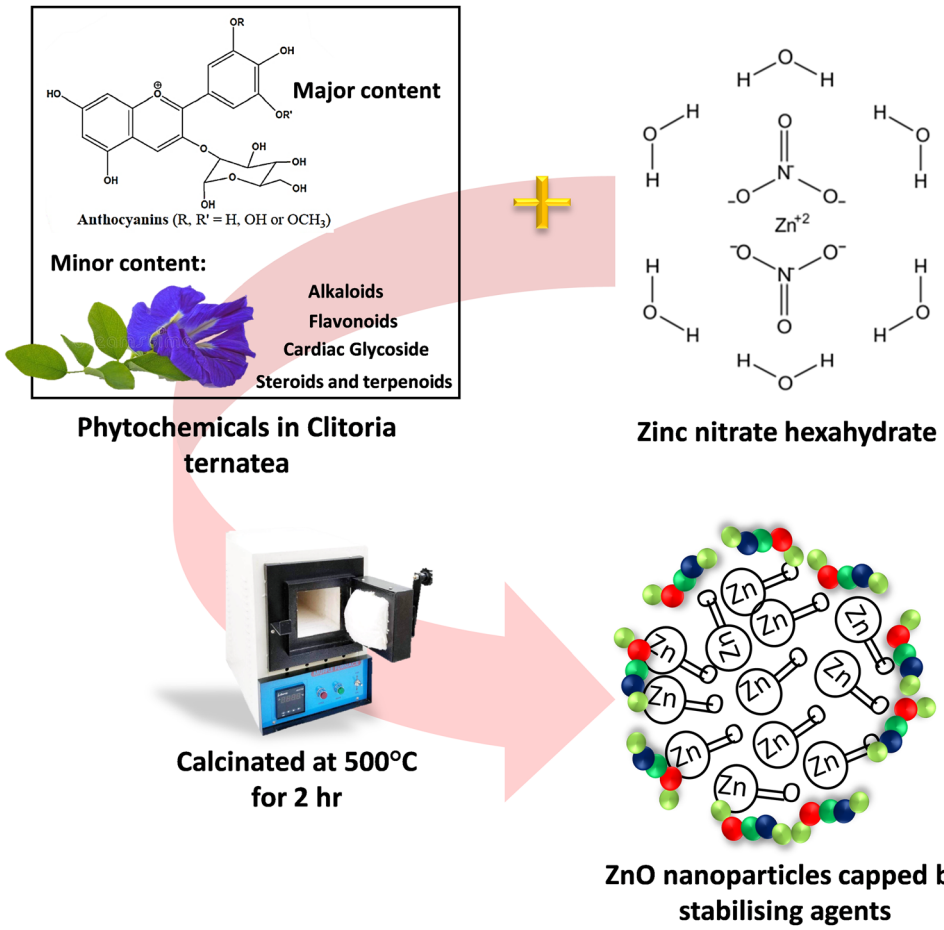

Scheme 1 Proposed mechanistic pathway for the biosynthesis of ZnO nanoparticles mediated by the Clitoria ternatea flower extract.

surface of the ZnO lattice. Adding these phytochemicals led to the enhancement in crystalline structure, promoting quick electron charge transfer.[42]

Raman spectral analysis was conducted for both samples to determine the Raman-active modes of the wurtzite hexagonal phase of the ZnO crystal, as confirmed in Fig. 1(b). The most intense peak at 438 cm^{-1} is attributed to oxygen vibration (E_{2H} mode). Its prominent asymmetry is related to lattice disorder and anharmonic phonon–phonon interactions. Polar phonons A1 and E1 present distinct frequencies for transverse-optical (TO) and longitudinal-optical (LO) phonons with A1(LO) and E1(LO) at 540 and 579 cm^{-1}, respectively. E1(TO) at 380 cm^{-1} and 2E2 at 332 cm^{-1} are attributed to further Raman active modes. The correlation of the Raman spectra with XRD data emphasizes the crystallinity and signature of the hexagonal wurtzite structure. Additionally, a change in intensity of CT-ZnO compared to ZnO indicates the successful formation of phytochemicals on the ZnO surface.[21,43,44]

Photoluminescence spectra demonstrated a wide emission band in the 370–520 nm range, as shown in Fig. 1(c). The emission intensity of CT-ZnO exhibited a prominent increase over that of the pristine ZnO, signifying improved radiative recombination. The emission peak in the range of 380 to 400 nm is attributed to the near-band-edge (NBE) emission of ZnO due to the recombination of free excitons. The broad visible emission at 450–520 nm is attributed to deep-level or defect-related emissions associated with vacant oxygen, zinc interstitials, or other intrinsic defects in the ZnO lattice. The enhancement in PL intensity in CT-ZnO is due to modification of surface parameters and may also be attributed to the interaction of phytochemicals, mainly anthocyanins, which influence the crystal growth.[45]

Absorbance and optical bandgap were examined using UV-vis spectra, as depicted in Fig. 1(d) and (e). The absorbance spectra of ZnO and CT-ZnO demonstrated greater absorption in the visible region at the wavelength of 368 nm, showcasing light-induced inter-band electronic transitions with visible light excitation.[46] By employing the Kubelka–Munk function $f(R)^2$ *vs.* energy, the desired band gap of the material was obtained, where CT-ZnO (3.12 eV) < ZnO (3.14 eV), as demonstrated in Fig. 1(e). CT-ZnO exhibited greater absorbance and reduced bandgap, indicating enhanced optical properties. This consideration suggests the additional formation of the lowest unoccupied molecular orbital due to the presence of phytochemicals on the ZnO lattice surface acting as capping/stabilizing agents, thereby enhancing the electron transfer and causing the red shift in UV emission.[46,47] The UV-Vis spectrum of CT flower extract was also examined Fig. S1(b); the diluted CT water

© 2026 The Author(s). Published by the Royal Society of Chemistry

Open Access Article. Published on 19 May 2026. Downloaded on 6/21/2026 8:54:41 PM.
This article is licensed under a Creative Commons Attribution-NonCommercial 3.0 Unported Licence.

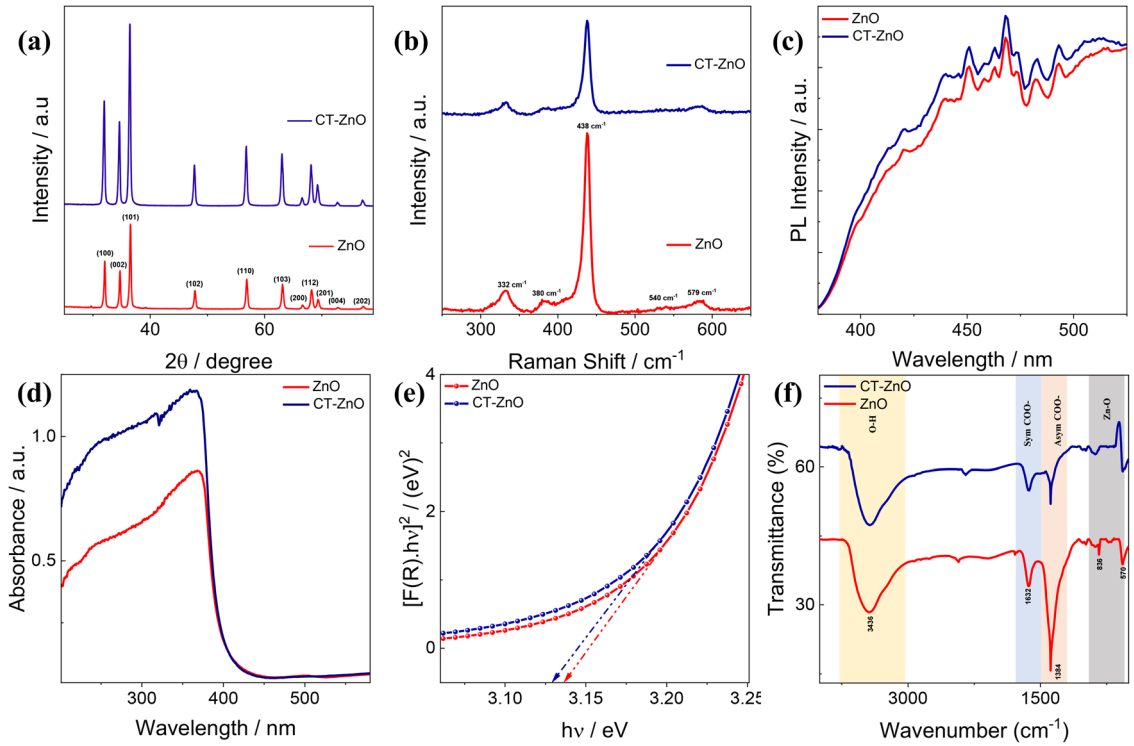

Fig. 1 (a) XRD patterns of ZnO and CT-ZnO. (b) Raman spectra of ZnO and CT-ZnO. (c) Photoluminescence spectra of ZnO and CT-ZnO. (d) UV-vis spectra of ZnO and CT-ZnO. (e) Optical energy bandgaps of ZnO and CT-ZnO. (f) FT-IR spectra of ZnO and CT-ZnO.

extract demonstrated an absorption band at 624 nm with an absorbance intensity of 1.26, which is attributed to the anthocyanin pigment present in CT flower, along with one more absorption band at 267 nm due to other colourless pigments.[48]

The functional groups present in both ZnO and CT-ZnO samples were identified using the FTIR technique, which recorded spectra within the 500–4000 cm^{-1} range. The spectra of the samples revealed unique, distinctive absorption bands, highlighted in Fig. 1(f). The O–H stretching vibrations of hydroxyl groups (–OH) associated with surface-adsorbed moisture on ZnO nanoparticles contribute to the broad absorption band observed in the 3436 cm^{-1} range.[49] Carbonate forms can be detected by the bands that lie between 1384 and 1632 cm^{-1}, leading to the symmetric and asymmetric vibrations of COO^{-} groups. Moreover, Zn–O stretching modes, an aspect of ZnO, give rise to the significant peaks that occur at 570 cm^{-1} and 836 cm^{-1}[50]. Overall, the reduction in intensity in the FTIR spectra of CT-ZnO indicates the presence of phytochemical functional groups from the CT extract, which are engaged in the reduction, capping, and stabilization of the nanoparticles, additionally validating the formation of ZnO.[51]

To elucidate the conductivity of a material, electrochemical characterisation was conducted utilising a three-electrode setup. As shown in Fig. 2(a), bare NF showed a minimum redox behaviour at 50 mV s^{-1} with the potential window of +0.2 V to +0.75 V *vs.* Ag/AgCl in 0.1 M KOH. On coating the substrate NF

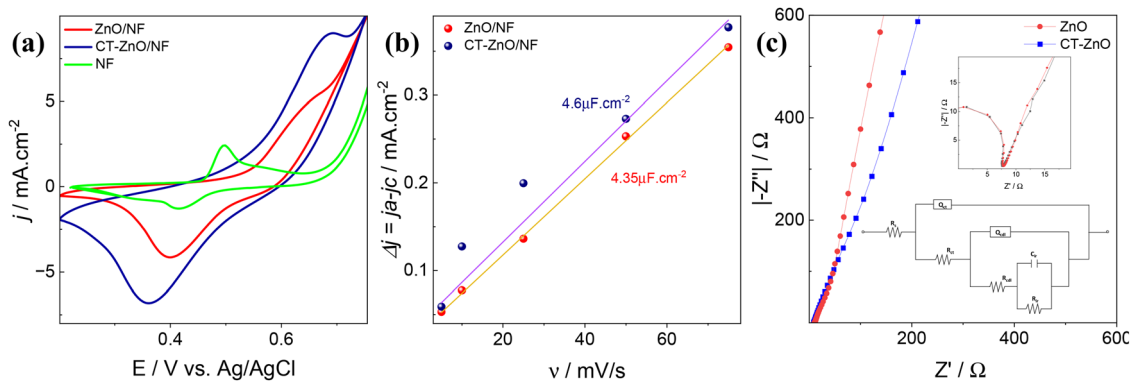

Fig. 2 (a) CV analysis of bare NF, ZnO/NF, and CT-ZnO/NF at a scan rate of 50 mV s^{-1} in 0.1 M KOH. (b) ECSA plots of ZnO/NF and CT-ZnO/NF. (c) EIS plot of ZnO and CT-ZnO, respectively, with the fitted circuit and zoomed in image of semicircle of EIS plot inset.

Open Access Article. Published on 19 May 2026. Downloaded on 6/21/2026 8:54:41 PM.
This article is licensed under a Creative Commons Attribution-NonCommercial 3.0 Unported Licence.

with pristine ZnO, a notable enhancement in current was observed in comparison with bare NF, signifying increased electrochemical characteristics owing to the semiconducting property of ZnO. Remarkably, the CT-ZnO exhibited tremendous enhancement in redox behaviour in comparison to pristine ZnO. This increase in redox behaviour may be related to the phytochemicals from the CT extract, which provide surface modifications and enhance charge-transfer kinetics, as proven in Fig. S2(a) and (b). Here, we can explore the number of electrons transferred during the oxidation process of ZnO and CT-ZnO, where the electron transfer rate is enhanced in CT-ZnO in comparison to pristine ZnO. The number of electrons transferred was found to be 0.38×10^{19} and 1.84×10^{19} for ZnO and CT-ZnO, respectively.[52,53] The improved electron-transfer characteristics imply that the biofunctionalized ZnO provides a highly conductive and active surface, favourable for biosensing applications.

As demonstrated in Fig. 2(b) and Fig. S3(a) and (b), the ECSA comparison of ZnO and CT-ZnO was analysed based on the double-layer capacitance obtained from CV analysis in the non-faradaic region. CT-ZnO (4.6 μF cm^{-2}) showed a higher C_{dl} value than pristine ZnO (4.35 μF cm^{-2}), demonstrating a greater surface area of 0.058 cm^2 and 0.054 cm^2, respectively, as shown in Table S2.[52,54,55] The enhanced surface area of CT-ZnO is attributed to bioactive phytochemicals from the flower extract, which facilitate charge-transfer kinetics, thereby leading to the improved sensitivity and electrocatalytic performance of CT-ZnO. Since the observed difference was relatively small, BET analysis was performed to accurately determine the specific surface area. The nitrogen adsorption–desorption isotherms Fig. S3(c) revealed that pristine ZnO had a specific surface area of 6.53 m^2 g^{-1}, whereas CT-ZnO had a higher surface area of 7.51 m^2 g^{-1}. Furthermore, both samples displayed type IV isotherms with a distinct hysteresis loop, indicating the presence of mesoporous structures. These mesopores facilitate enhanced ion mobility through improved interactions with the electrolyte, thereby contributing to superior electrocatalytic performance.

EIS was employed in a three-electrode setup to examine the conductivity and interfacial behaviour of ZnO/NF and CT-ZnO/NF electrodes. The equivalent circuit model, including solution resistance (R_s), double-layer resistance (R_{cdl}), charge-transfer resistance (R_{ct}), and internal resistance (R_{ir}), was adapted to the Nyquist plots in Fig. 2(c). Relevant data about the effectiveness of the electrode is likely to be determined from the electrochemical parameters shown in Table S3. In comparison with ZnO/NF, CT-ZnO/NF displayed noticeably lower R_s and R_{ct} values, highlighting its superior electrochemical activity and improved charge-transfer efficiency.

Morphological characterisation was conducted using FESEM, and the elemental analysis was carried out using EDAX. Fig. 3(a) shows the FESEM analysis of ZnO, exhibiting a hexagonal morphology, which is characteristic of wurtzite-structured ZnO. Fig. 3(e), which reflects CT-ZnO, reveals a noticeable change in morphology, with the hexagonal shape eventually transitioning to an ellipsoidal form. This implies that the inclusion of the floral extract affects the ZnO surface expansion profile. Furthermore, the elemental composition of the synthesised material was examined by EDAX, as shown in Fig. S4(a) and (b), which revealed

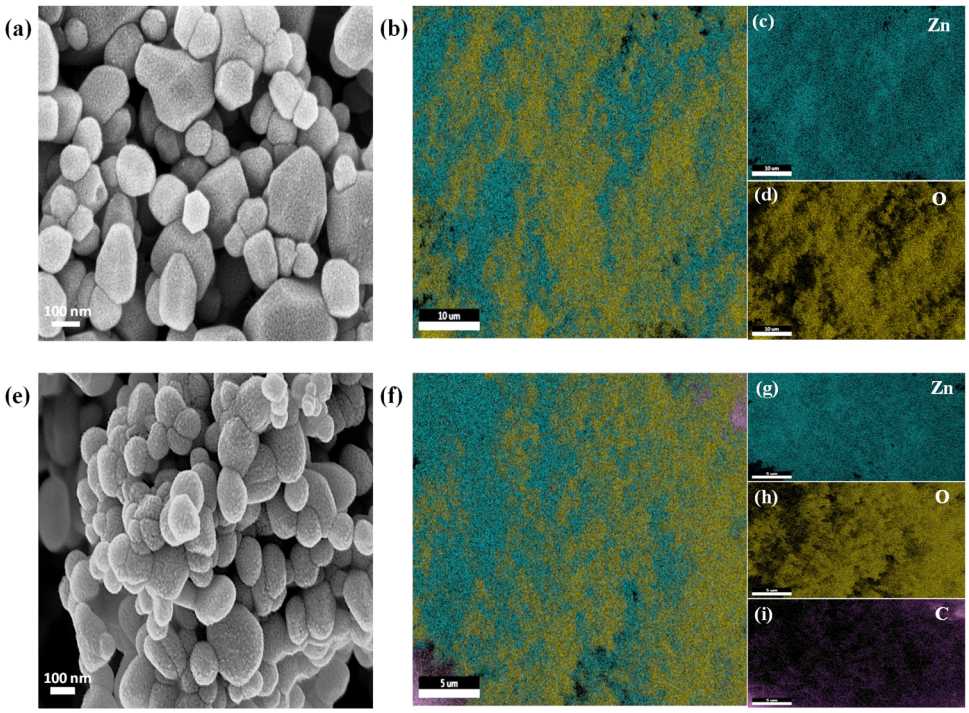

Fig. 3 (a) FESEM image of ZnO. (b) Elemental analysis of ZnO. Elemental mapping images of (c) Zn and (d) O. (e) FESEM image of CT-ZnO. (f) Elemental analysis of CT-ZnO. Elemental mapping images of (g) Zn, (h) O, and (i) C.

© 2026 The Author(s). Published by the Royal Society of Chemistry

Open Access Article. Published on 19 May 2026. Downloaded on 6/21/2026 8:54:41 PM. This article is licensed under a Creative Commons Attribution-NonCommercial 3.0 Unported Licence.

distinct peaks corresponding to Zn and O, supporting the material's purity. The CT-ZnO EDAX displayed an additional peak ascribed to C (carbon), which appeared due to the addition of organic phytochemicals on the ZnO surface.

EDAX colour mapping was conducted, which explicitly demonstrated the spatial distribution of the individual components, as depicted in Fig. 3(b)–(d) for ZnO and Fig. 3(f)–(i) for CT-ZnO. To ensure uniform coverage across the sample surface, each component was depicted in an identifiable shade. This suggests that the phytochemicals have been effectively embedded without drastically affecting the crystal framework. The average size of the particles was found to be 14.7 ± 3.8 nm for pristine ZnO and 11.8 ± 2.7 nm for CT-ZnO, as presented in Fig. S5(a) and (b). The considerably smaller particle size of CT-ZnO suggests a larger surface area due to the capping effect that inhibits growth and improves the surface-to-volume ratio.[56]

Accordingly, the CT-ZnO sample was further investigated using HR-TEM, as shown in Fig. 4(a)–(c). The images reveal that the native hexagonal morphology of ZnO was transformed into an ellipsoidal structure, consistent with the observations from SEM analysis. The lattice fringes corresponding to adjacent crystallographic planes were clearly resolved, exhibiting a uniform interplanar spacing of 0.25 nm, indexed to the (101) plane of ZnO. This confirms the preservation of the hexagonal wurtzite crystal structure and is in good agreement with the XRD results. Furthermore, the well-defined and continuous lattice fringes without noticeable distortion indicate the retention of the intrinsic crystallinity of ZnO. This structural integrity suggests that the phytochemicals present during synthesis likely act as effective capping or stabilizing agents on the nanoparticle surface.

To pinpoint and estimate the probability of metal ions in improving the electrochemical characteristics of the synthesised material, the elemental composition of the CT flower extract was examined using ICP-MS. The outcomes shown in Table 1 and Fig. S6(a)–(e) indicate a greater potassium (K) concentration of 39.03 ppm in 30 mL of extract, with 468.36 ppm in the total concentration of flower extract. Potassium is vital in enhancing ionic conductivity and assisting electron transfer, affecting the electrochemical performance of CT-ZnO.[55]

Additionally, sodium (Na) was observed to be 2.65 ppm (31.8 ppm), whereas magnesium (Mg), iron (Fe), and calcium (Ca) were identified in minor quantities, that is, 1.14 ppm (13.68 ppm), 0.18 ppm (2.16 ppm), and 0.07 ppm (0.84 ppm), respectively. These trace elements, especially Mg and Fe, may impact the materials' behaviour by fostering catalytic activity or by altering the electronic structure of the composite. The appearance of these elements demonstrates that the presence of the bioavailable metal ions in the flower extract interacts with the surface of the ZnO lattice, modulating the functional improvement of the nanomaterial.[55]

Table 1 Elemental composition of the *Clitoria ternatea* flower extract

Elements in the flower extract	Concentration in the 30 mL extract (ppm)	Total concentration in the extract (ppm)
K	39.03	468.36
Na	2.65	31.8
Mg	1.14	13.68
Fe	0.18	2.16
Ca	0.07	0.84

A sequence of chemical tests was conducted to determine the significant bioactive compounds in CT flower extract, as demonstrated in Fig. S7(a)–(e). The UV-vis spectra of the CT flower extract have already confirmed the strong presence of anthocyanin, a phenolic compound, which is further justified by the formation of a red colour upon undergoing the ferric chloride test. Alkaloids were detected utilising Mayer's reagent, which resulted in the solution turning white, signifying a positive outcome. Flavonoids were identified by employing the alkaline reagent test, where the formation of a yellow colour confirmed their presence. The Salkowski test yielded a favourable outcome, with the formation of a reddish upper layer, and the presence of terpenoids and steroids was confirmed. Furthermore, a Keller-Kiliani test was performed to detect the presence of cardiac glycoside, which also yielded a positive result, due to the formation of a brownish upper layer and a reddish bottom layer. These basic phytochemical tests indicate the presence of bioactive elements in the flower extract, which are known for their antioxidant and bioactive potential.[57]

XPS was conducted to investigate the elemental composition and chemical states of the CT-ZnO nanostructures. The wide-scan survey spectrum Fig. 5(a) revealed the presence of Zn, O, and C as the major elements, confirming the formation of zinc oxide and successful surface modification by bio-organic

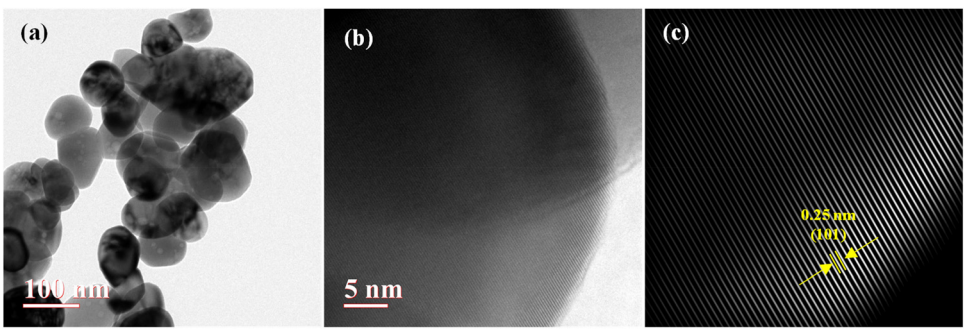

Fig. 4 (a)–(c) HR-TEM images of CT-ZnO.

Open Access Article. Published on 19 May 2026. Downloaded on 6/21/2026 8:54:41 PM.
This article is licensed under a Creative Commons Attribution-NonCommercial 3.0 Unported Licence.

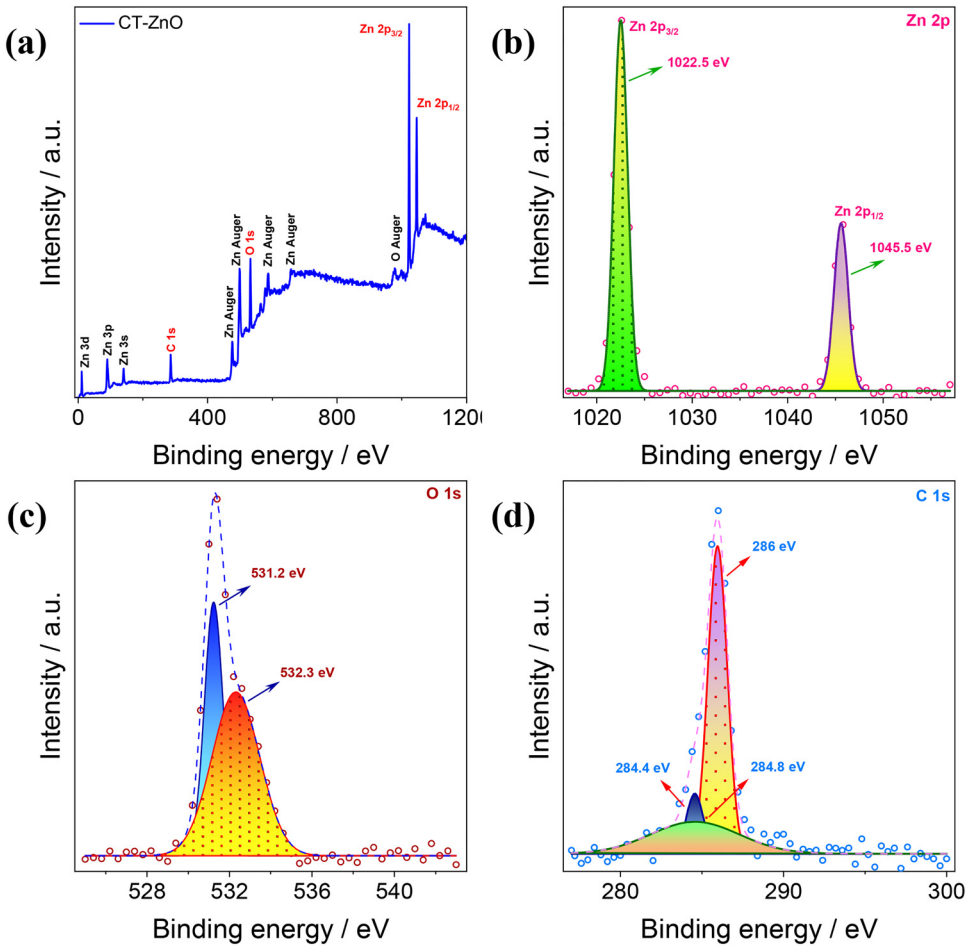

Fig. 5 XPS analysis of CT-ZnO: (a) survey, (b) Zn 2p, (c) O 1s, and (d) C 1s spectra.

components from the flower extract. The high-resolution Zn 2p spectrum, shown in Fig. 5(b), exhibited two distinct peaks located at binding energies of approximately 1022.5 eV and 1045.5 eV, corresponding to the Zn $2p_{3/2}$ and Zn $2p_{1/2}$ transitions, respectively. The observed spin–orbit splitting of ~23 eV is characteristic of Zn^{2+} in the ZnO lattice, with no satellite peaks indicating the absence of metallic zinc or other oxidation states.[58,59]

The O 1s core-level spectrum in Fig. 5(c) was deconvoluted into two main components. The dominant peak at ~531.2 eV is attributed to lattice oxygen (O^{2-}) in ZnO, while the shoulder at ~532.3 eV corresponds to hydroxyl groups and/or oxygen atoms bonded to carbon (C–O or C═O), indicative of organic functionalities introduced by the flower extract. The C 1s spectrum in Fig. 5(d) displayed a primary peak at 284.4 eV, which is assigned to adventitious carbon (C–C/C–H). Additional components observed at ~284.8 eV and ~286 eV are associated with C–O and O–C═O functional groups, respectively. These oxygenated carbon species further confirm the existence of phytochemicals from the flower extract on the ZnO surface. Collectively, the XPS results validate the successful synthesis of CT-ZnO and its surface functionalization with bio-organic compounds from the flower extract, which may enhance its physicochemical properties for potential sensing applications.[59]

In comparison to the CV study, to understand the electrochemical properties of CT-ZnO/NF and ZnO/NF, a scan rate study was employed, as shown in Fig. 6(a) and Fig. S8(a), respectively, ranging from 5 to 120 mV s^{-1} in 0.1 M KOH. The main objective of this study is to note the anodic and cathodic peak currents. The results highlighted a tremendous enhancement in both redox peak currents with increasing scan rates. This enhancement is mainly due to the resulting diffusion layer formation. During the lower scan rates, a thicker diffusion layer is formed, which prevents the constant interaction of electroactive species with the electrode surface, thereby reducing both redox peak currents. Conversely, when it comes to enhanced scan rate, a contrary effect is observed. As the scan rate increases, the anodic peak relocates towards positive potential while the cathodic peak relocates towards negative potential. Remarkably, a linear resemblance between the square root of the scan rate and redox characteristics of CT-ZnO/NF is demonstrated in the inset plot of Fig. 6(a). This observational result implies the restriction caused by the diffusion layer towards the electroactive species, suggesting the electron transfer persists through an outer sphere mechanism.

The experimental findings underscore the promising potential of the developed platform for the fabrication of an

© 2026 The Author(s). Published by the Royal Society of Chemistry

Open Access Article. Published on 19 May 2026. Downloaded on 6/21/2026 8:54:41 PM.
This article is licensed under a Creative Commons Attribution-NonCommercial 3.0 Unported Licence.

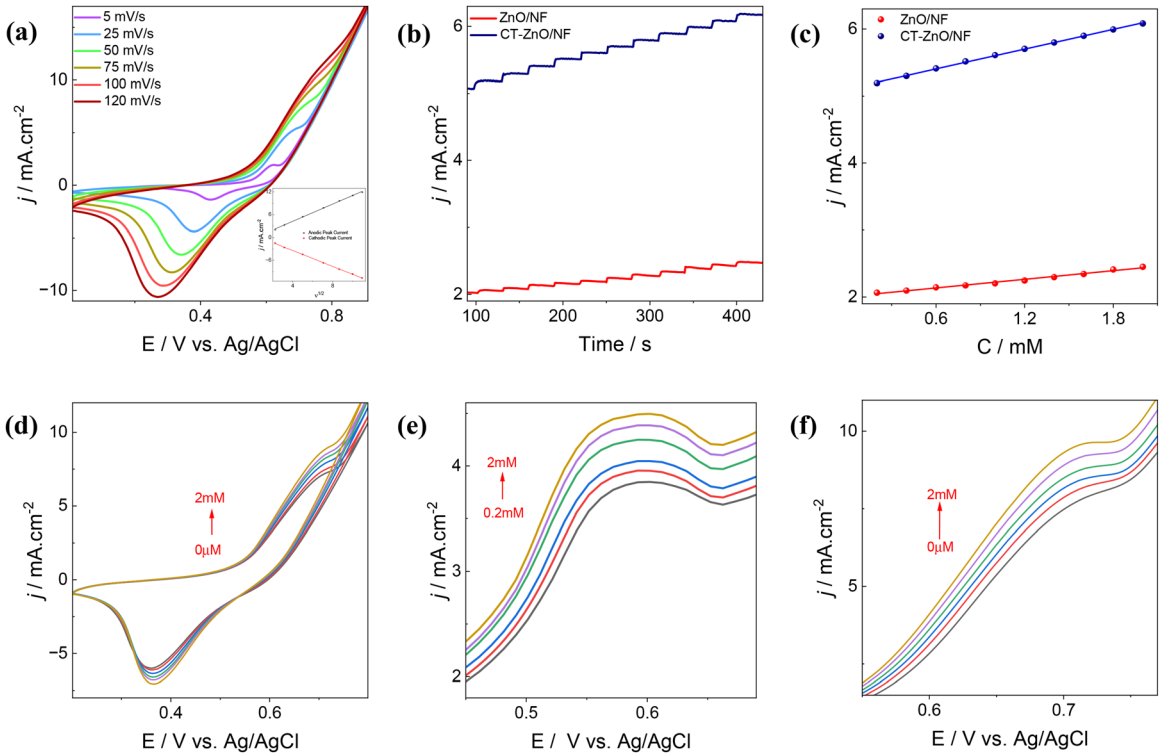

Fig. 6 (a) Scan rate study of CT-ZnO/NF from 5 to 120 mV s^{-1} in 0.1 M KOH. The cathodic and anodic peak currents are inserted as a function of the square root of the scan rate (inset). (b) CT-ZnO/NF and ZnO/NF CA studies performed in a 0.1 M KOH solution. The experiments were conducted with stirring and an applied potential of +0.69 and +0.64 V, respectively. (c) Calibration plots of CT-ZnO/NF and ZnO/NF to estimate cholesterol. (d) Evaluation of successive additions for CT-ZnO/NF at a scan rate of 50 mV s^{-1}. (e) Analysis of the electrochemical response to subsequent cholesterol additions *via* DPV study of CT-ZnO/NF. (f) LSV study of CT-ZnO/NF to analyse the electrochemical reaction to successive cholesterol additions.

enzyme-free amperometric sensor tailored for cholesterol detection. The sensors based on ZnO/NF and CT-ZnO/NF were systematically evaluated *via* CA measurements across a cholesterol concentration range of 0 μM to 2 mM, as depicted in Fig. 6(b). All measurements were conducted at a fixed potential of +0.64 and +0.69 V for ZnO/NF and CT-ZnO/NF, respectively, under continuous stirring, with current responses recorded at 30 s intervals. A clear and proportional increase in the anodic current was observed with each incremental addition of cholesterol, indicative of effective electrochemical sensing. This behaviour is attributed to the enhanced formation of the diffusion layer at the electrode–electrolyte interface, facilitating improved electron transfer kinetics. The calibration curve, Fig. 6(c), demonstrated a strong linear relationship over the tested concentration range.

The electrochemical behaviour depicted in Fig. 6(d) and Fig. S8(b) illustrates the effect of incremental cholesterol addition to a 0.1 M KOH solution within a linear range of 0 μM to 2 mM at a scan rate of 50 mV s^{-1} of CT-ZnO/NF and ZnO/NF, respectively. A progressive enhancement in the anodic peak of the CV curves was observed with increasing cholesterol concentration, signifying efficient electrocatalytic oxidation of cholesterol. This increase in current response is attributed to the increase in the analyte's diffusion layer at the electrode interface, which facilitates greater availability of cholesterol molecules for oxidation, thereby amplifying the anodic signal. For a clearer interpretation, Fig. S8(c) depicts the pronounced oxidation and reduction peaks of CT-ZnO with cholesterol observed at a scan rate of 50 mV s^{-1}. Furthermore, the DPV analysis of CT-ZnO/NF demonstrated excellent repeatability, confirming the reliability of this method for cholesterol sensing. As shown in Fig. 6(e) and Fig. S8(d), a clear linear response was observed over a concentration range of 0 μM to 2 mM, using a scan rate of 10 mV s^{-1} CT-ZnO/NF and ZnO/NF, respectively. Incremental additions of cholesterol to 0.1 M KOH resulted in distinct current changes, highlighting the sensor's high sensitivity.

Complementing the DPV and successive addition studies, LSV was conducted to further assess the electrochemical performance of CT-ZnO/NF and ZnO/NF towards cholesterol detection, as shown in Fig. 6(f) and Fig. S8(e). The LSV measurements were carried out in 0.1 M KOH with cholesterol concentrations ranging from 0 μM to 2 mM at a scan rate of 50 mV s^{-1}. A consistent increase in anodic current with increasing cholesterol concentration was observed, indicative of efficient electrocatalytic oxidation. These results further validate the sensitivity and reliability of CT-ZnO/NF as a promising electrode material for nonenzymatic cholesterol sensing.

The long-term durability of the CT-ZnO/NF and ZnO/NF electrodes was evaluated in the presence of 2 mM cholesterol over 100 continuous cycles. As shown in Fig. 7(a), the electrode retained approximately 98.8% of its initial performance,

Open Access Article. Published on 19 May 2026. Downloaded on 6/21/2026 8:54:41 PM.
This article is licensed under a Creative Commons Attribution-NonCommercial 3.0 Unported Licence.

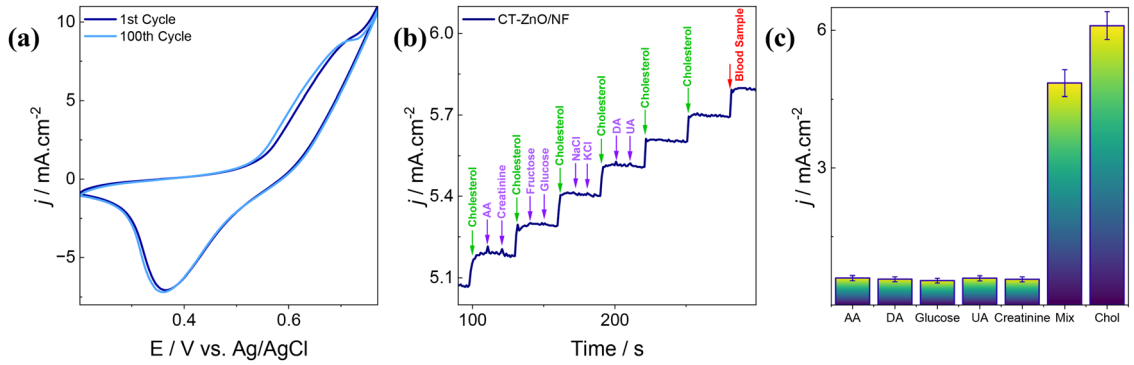

Fig. 7 (a) CT-ZnO/NF CV plots for 100 cycles at an applied scan rate of 50 mV s^{-1} in a 0.1 M KOH solution with 2 mM cholesterol. (b) Interference analysis of CT-ZnO/NF at a potential of +0.69 V with stirring to assess its response to multiple interfering species. (c) DPV interference evaluation of CT-ZnO/NF with a 50 mV pulse amplitude and a scan rate of 10 mV s^{-1}.

indicating excellent structural and functional stability. This is comparable to the stability of 97.9% demonstrated by ZnO/NF, as depicted in Fig. S8(f). These findings highlight the improved electrochemical stability and performance of CT-ZnO/NF electrodes, reinforcing their potential for reliable application in nonenzymatic cholesterol biosensing.

Selectivity is one of the key attributes of an effective biosensor. To assess the selectivity of the CT-ZnO/NF and ZnO/NF electrodes for cholesterol detection, an interference study was conducted using CA under stirring conditions at a constant potential of +0.69 V and +0.64 V, as shown in Fig. 7(b) and Fig. S8(g). The electrode's response was tested in 0.1 M KOH in the presence of common interfering species such as ascorbic acid (AA), dopamine (DA), uric acid (UA), glucose, fructose, NaCl, KCl, and creatinine at concentrations of 0.5 mM, Fig. 7(b) and 1 mM, Fig. S8(i) for CT-ZnO. The introduction of human blood serum containing cholesterol increased the current response, validating the electrode's sensitivity to detect cholesterol. The current response exhibited a distinct stepwise increase only upon the addition of cholesterol, while the introduction of the interfering species caused negligible changes in current. This behaviour indicates a high degree of selectivity of the CT-ZnO/NF electrode toward cholesterol.

To corroborate the interference results, DPV analysis was also performed, as illustrated in Fig. 7(c). The DPV results included measurements for individual interfering species, a mixture of interferents with cholesterol, and cholesterol alone. Notably, the interfering species caused minimal current variations, whereas cholesterol induced a pronounced increase in the current response. These findings clearly demonstrate the CT-ZnO/NF electrode's excellent selectivity, sensitivity, and reliability, making it a promising candidate for nonenzymatic cholesterol biosensing applications.

The fundamental PEC oxidation pathway of biomolecules is expressed in Fig. 8. Adsorption of the intended biomolecules in

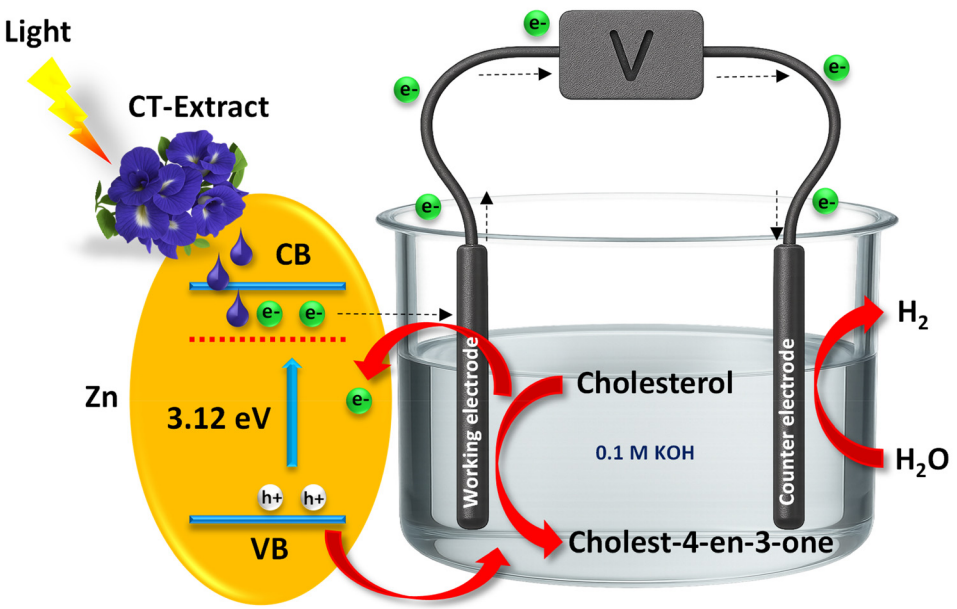

Fig. 8 Probable schematic description of a cholesterol biosensor in accordance with PEC.

© 2026 The Author(s). Published by the Royal Society of Chemistry

Open Access Article. Published on 19 May 2026. Downloaded on 6/21/2026 8:54:41 PM. This article is licensed under a Creative Commons Attribution-NonCommercial 3.0 Unported Licence.

PEC biosensing generates an enhanced photocurrent with a value proportionate to the concentration of the biomolecules. The incorporation of phytochemicals derived from CT flower extract, including anthocyanins, flavonoids, and phenolic compounds, significantly influences the photoelectrochemical behavior of the system. Owing to their π-conjugated structures and functional groups such as –OH and –C═O, these biomolecules act as effective photosensitizers by absorbing incident light and facilitating electron excitation.[60] Consequently, they promote rapid electron transfer to the conduction band, suppress electron–hole recombination, and thereby enhance the overall photoelectrochemical response.

The PEC mechanism is as outlined below: (a) the CT-ZnO/NF substrate absorbs light, leading to electron–hole pairs; (b) charges separate and migrate, with holes migrating towards the electrolyte and electrons towards the working electrode (WE). When in contact with light, holes in the valence band lead biomolecules to oxidise, while electrons that originate in the conduction band migrate from the WE to the Pt counter electrode. Here, oxidation of cholesterol forms cholest-4-en-3-one, which promotes electron transport and improves sensor sensitivity. This constructed approach facilitates the PEC biosensor's superior effectiveness and stability.[21,61]

The Laviron equation (eqn (1)) was used to determine the number of electrons that contribute to cholesterol oxidation, as follows:

$$\text{Slope} = \frac{RT}{F\alpha n} \quad (1)$$

As illustrated in Fig. S9(a), the constants R (8.314 J mol^{-1} K^{-1}), T (300 K), F (96 480 C mol^{-1}), and the transfer coefficient (α = 0.3) were integrated into the slope of ln(ν) *vs.* anodic peak potential (E). The outcome shows an exchange of 2 electrons from the calculation, demonstrating that during electro-oxidation, cholesterol transfers two electrons.

The fabricated material's optoelectronic qualities were further investigated *via* a PEC study carried out under illumination by light. CV measurements were performed for both CT-ZnO/NF and ZnO/NF electrodes under dark and illuminated conditions to assess their photoelectrochemical behaviour, Fig. 9(a) and Fig. S10(a), respectively. Upon illumination, a marked enhancement in both anodic and cathodic currents was observed, which can be attributed to the efficient generation of photoinduced electron–hole pairs. The increased charge carrier density under light exposure facilitates improved redox kinetics at the electrode–electrolyte interface. Notably, the CT-ZnO/NF electrode demonstrated a more pronounced photocurrent response, suggesting enhanced light absorption and superior charge separation efficiency, likely due to the structural or electronic modifications by CT functionalization.

The results achieved highlight the ability of the approach to develop an amperometric sensor intended solely for cholesterol assessment. A detailed study on enzyme-less cholesterol sensing was carried out, adopting CT-ZnO/NF as the effective electrode. The linear behaviour of the sensor had been evaluated in conditions with and without light, applying cholesterol concentrations that varied from 0 μM to 2 mM, Fig. 9(b). The amperometric reading was recorded at intervals of thirty seconds while measurement procedures were made at a fixed potential of +0.69 V, while stirring constantly. The electrode's sensitivity to cholesterol has been proven by an appropriate spike in anodic current with every addition of cholesterol. This observation is facilitated by the enhanced diffusion layer at the electrode surface. Similarly, amperometric measurements were performed using the ZnO/NF electrode at an applied potential of +0.69 V, and the corresponding calibration curve is presented in Fig. S10(b) and (c).

Excellent linearity has been verified across the tested range of concentrations in the corresponding calibration curve, Fig. 9(c). The sensitivity of ZnO/NF with and without light modes was 387 μA mM^{-1} cm^{-2} and 215.6 μA mM^{-1} cm^{-2}, respectively, with the LOD being 99 μM and 66 μM, while the LOQ was 330 μM and 220 μM, respectively. CT-ZnO exhibited a tremendous enhancement in the sensing ability of the sensor with and without light, being 956 μA mM^{-1} cm^{-2} and 492.5 μA mM^{-1} cm^{-2}, respectively. In addition to a rapid response time of 2 s Fig. S8(h), the LOD results were 28 μM and 35 μM, while the LOQ values obtained were found to be 95 μM and 110 μM with and without illumination.

An in-depth analysis of charge carrier separation and transfer efficiency was performed by monitoring the photocurrent response under periodic ON–OFF light conditions for a total visible light irradiation duration of 2000 s. As supported by the literature, ZnO demonstrates excellent potential as a potent photocatalyst owing to its distinct nano morphologies.[62] The ZnO/NF electrode demonstrated an enhancement in photocurrent response, as shown in Fig. S10(d), whereas the CT-ZnO/NF electrode demonstrated a distinct and reproducible photo response, with the current density increasing from ∼7.22 mA to ∼7.42 mA under a constant bias voltage of +0.69 V upon illumination, as illustrated in Fig. 9(d). This enhancement indicates improved generation and separation of photoinduced charge carriers within the CT-ZnO/NF system, confirming the material's high reproducibility, operational stability, and suitability for practical photoelectrochemical applications. The selectivity of CT-ZnO nanoparticles (Fig. S10(e)) in the presence of light at +0.69 V was also analysed to demonstrate the negligible interaction with different interfering species, thereby showcasing the material's excellent selectivity toward cholesterol.

The CT-ZnO/NF electrode was employed for the practical determination of cholesterol in human blood serum samples obtained from a clinic in the presence and absence of light, Fig. S12(a)–(f). Prior to the experiment, the serum sample underwent strong alkaline hydrolysis followed by neutralization and dilution by electrolyte, where the cholesterol esters were converted to free cholesterol. This ensured that the results obtained from electrochemical determination correlate with the total cholesterol determined clinically. The measured cholesterol levels demonstrated excellent agreement with the clinically estimated values, exhibiting a recovery range of 88%–93%, as summarised in Table 2. These results affirm the analytical reliability and practical applicability of the CT-ZnO/NF electrode for real-sample analysis.

Open Access Article. Published on 19 May 2026. Downloaded on 6/21/2026 8:54:41 PM.
This article is licensed under a Creative Commons Attribution-NonCommercial 3.0 Unported Licence.

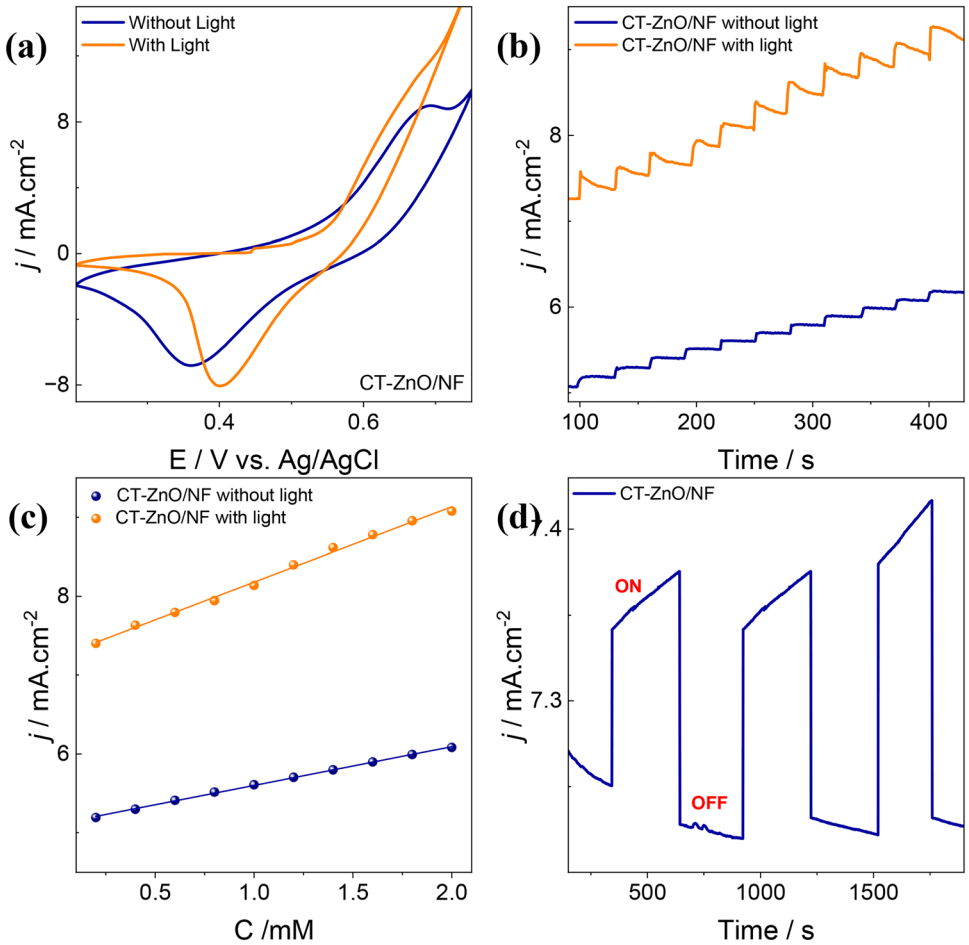

Fig. 9 (a) CV analysis of CT-ZnO/NF with and without light at a scan rate of 50 mV s^{-1}. (b) CA investigation of CT-ZnO/NF performed in a 0.1 M KOH solution, while stirring, along with a potential of +0.69 V. (c)Calibration plot of CT-ZnO/NF to estimate the concentration of cholesterol. (d) Photocurrent analysis of CT-ZnO/NF in dark and illuminated modes at a potential of +0.69 V.

Table 2 Real human serum sample analysis

Patient	Gender	Clinically tested result (mg dL^{-1})	Experimental result (mg dL^{-1})	% Accuracy
Patient 1	Female	236	209	88.5
Patient 2	Male	224	203.7	90.9
Patient 3	Male	170	158	92.9
Patient 4	Female	196	182	92.8
Photoelectrochemical blood serum detection				
Patient 1	Female	236	211.5	89.6
Patient 2	Male	224	204.2	91.2

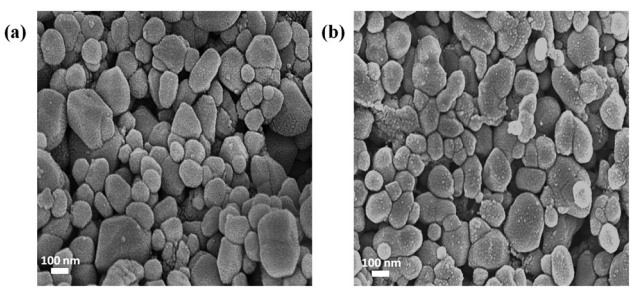

Fig. 10 FESEM images of (a) ZnO/NF and (b) CT-ZnO/NF after treatment with 2 mM of cholesterol.

FESEM analysis was conducted for both ZnO and CT-ZnO samples, Fig. 10(a) and (b), following treatment with 2 mM cholesterol to investigate morphological changes resulting from cholesterol interaction after a long-term study of 100 cycles. The post-treatment images revealed no discernible alteration in surface morphology, but rather small white dots were observed due to cholesterol oxidation in both samples when compared to their untreated counterparts. The structural integrity and surface features remained intact, indicating that the cholesterol interaction primarily occurs at the electrochemical interface without inducing significant morphological transformations. This suggests that the sensing mechanism is governed predominantly by surface adsorption and electron transfer processes rather than any structural modification of the electrode material.

Furthermore, reproducibility was validated by testing three independently prepared CT-ZnO/NF electrodes under identical conditions at the scan rate of 50 mV s^{-1} in 0.1 M KOH in the presence and absence of light Fig. S11(a) and (b), respectively. The resulting current responses were consistent across all electrodes, confirming excellent fabrication reproducibility.

© 2026 The Author(s). Published by the Royal Society of Chemistry

Open Access Article. Published on 19 May 2026. Downloaded on 6/21/2026 8:54:41 PM. This article is licensed under a Creative Commons Attribution-NonCommercial 3.0 Unported Licence.

Moreover, the long-term stability of the CT-ZnO/NF electrode was assessed over 90 days, as depicted in Fig. S11(c). The electrode maintained stable current responses with only a slight decline, indicating no significant degradation in performance. These results collectively demonstrate the CT-ZnO/NF electrode's remarkable stability, reproducibility, and sustained catalytic activity, emphasising its potential for reliable and consistent nonenzymatic cholesterol sensing applications.

5. Conclusions

We have reported the successful phytochemical-assisted synthesis of ZnO nanoparticles incorporating *Clitoria ternatea* floral extract, as a sustainable and effective cholesterol-sensing platform that functions as a source of reduction and capping. Employing a wet chemical technique, ZnO and CT-ZnO were synthesised and coated on NF substrates. CT-ZnO/NF stood out owing to a greater surface area, enhanced electron flow kinetics, and improved photocatalytic activity. A wide linear detection range (0 μM–2 mM), a low detection limit (28 μM), a quick reaction time (2 s), and excellent sensitivity (956 μA mM^{-1} cm^{-2}) have been proven by the PEC evaluations employing the CT-ZnO/NF electrode. Furthermore, the electrode displayed notable durability against interference from prevalent biological species and outstanding reproducibility. Its practical significance for real-time clinical diagnostics was further emphasised by the electrode's exceptional long-term stability, which maintained approximately 98.8% efficiency over 90 days and verified accuracy in human serum samples. The synergistic significance of the green-engineered approach is made clear by its incorporation of phytochemicals, which not only enable a sustainable, non-toxic, biocompatible, stable morphology and eco-friendly synthetic process but also boost the material's surface activity and charge transfer capabilities. Nevertheless, even if the green synthesis approach is environmentally friendly and sustainable, it might prove challenging to accomplish scalability and batch-to-batch reproducibility for large-scale production.

Author contributions

Sushmitha S: writing–original draft, visualization, methodology, investigation, and conceptualization. Lavanya Rao: writing–review and editing, visualization, investigation, and conceptualization. Mahesha P Nayak: visualization and investigation. Shreeganesh Subraya Hegde: writing–review and editing. Badekai Ramachandra Bhat: writing–review and editing, supervision, and project administration.

Conflicts of interest

The authors declare that they have no known competing financial interests or personal relationships that could have appeared to influence the work reported in this paper.

Data availability

All characterization data and raw experimental results are included within the manuscript and supplementary information (SI). Supplementary information is available. See DOI: https://doi.org/10.1039/d6ma00056h.

The additional relevant data supporting the findings of this study are available from the corresponding author upon reasonable request.

Acknowledgements

The author (SS) expresses sincere gratitude to the Endodiab Clinic, Mangalore, for the provision of blood serum samples and extends appreciation to the National Institute of Technology Karnataka, Surathkal, for their invaluable assistance in supporting this research. Special thanks are also directed to the Central Research Facility (CRF), NITK, for offering the essential characterization facilities for the successful completion of this work.

References

1 J. W. Gofman, F. Lindgren, H. Elliott, W. Mantz, J. Hewitt, B. Strisower, V. Herring and T. P. Lyon, *Science*, 1950, **111**, 166–186.
2 D. S. Schade, L. Shey and R. P. Eaton, *Endocr. Pract.*, 2020, **26**, 1514–1523.
3 H. M. Yadav, J.-D. Park, H.-C. Kang and J.-J. Lee, *Chemosensors*, 2021, **9**, 98.
4 B. Kumar, S. Poddar and S. K. Sinha, *J. Iran. Chem. Soc.*, 2022, **19**, 4093–4116.
5 V. Narwal, R. Deswal, B. Batra, V. Kalra, R. Hooda, M. Sharma and J. S. Rana, *Steroids*, 2019, **143**, 6–17.
6 X. T. Nguyen, Y. Ho, Y. Li, R. J. Song, K. H. Leung, S. U. Rahman, A. R. Orkaby, J. L. Vassy, D. R. Gagnon, K. Cho, J. M. Gaziano and P. W. F. Wilson, *J. Am. Heart Assoc.*, 2023, **12**, e030496.
7 M. Ameen Sha, P. C. Meenu, H. Haspel and Z. Kónya, *RSC Adv.*, 2024, **14**, 24561–24573.
8 W.-C. Lee, K.-B. Kim, N. G. Gurudatt, K. K. Hussain, C. S. Choi, D.-S. Park and Y.-B. Shim, *Biosens. Bioelectron.*, 2019, **130**, 48–54.
9 H. M. Yadav, J.-D. Park, H.-C. Kang and J.-J. Lee, *Chemosensors*, 2021, **9**, 98.
10 Y.-J. Lee and J.-Y. Park, *Biosens. Bioelectron.*, 2010, **26**, 1353–1358.
11 P. Mohankumar, J. Ajayan, T. Mohanraj and R. Yasodharan, *Measurement*, 2021, **167**, 108293.
12 S. Sushmitha, S. S. Hegde, L. Rao, G. Varsha and B. R. Bhat, *Sens. Diagn.*, 2026, **5**, 8–25.
13 S. Sushmitha, S. Ray, L. Rao, M. P. Nayak, K. Carva and B. R. Bhat, *RSC Adv.*, 2025, 15, 34176–34190.
14 A. Devadoss, P. Sudhagar, C. Terashima, K. Nakata and A. Fujishima, *J. Photochem. Photobiol., C*, 2015, **24**, 43–63.

Open Access Article. Published on 19 May 2026. Downloaded on 6/21/2026 8:54:41 PM. This article is licensed under a Creative Commons Attribution-NonCommercial 3.0 Unported Licence.

15 H. Han, P. Sudhagar, T. Song, Y. Jeon, I. Mora-Seró, F. Fabregat-Santiago, J. Bisquert, Y. S. Kang and U. Paik, *Chem. Commun.*, 2013, **49**, 2810.
16 L. Ge, Q. Liu, N. Hao and W. Kun, *J. Mater. Chem. B*, 2019, **7**, 7283–7300.
17 M. Grätzel, *Nature*, 2001, **414**, 338–344.
18 Z. Kang, X. Yan, Y. Wang, Y. Zhao, Z. Bai, Y. Liu, K. Zhao, S. Cao and Y. Zhang, *Nano Res.*, 2016, **9**, 344–352.
19 W.-W. Zhao, J.-J. Xu and H.-Y. Chen, *Chem. Soc. Rev.*, 2015, **44**, 729–741.
20 Y. Gao, Z. Yu, L. Huang, Y. Zeng, X. Liu and D. Tang, *Anal. Chem.*, 2023, **95**, 9130–9137.
21 L. Rao, J. D. Rodney, A. Joy, C. Shivangi Nileshbhai, A. James, S. Sushmitha, F. Joyline Mascarenhas, N. K. Udayashankar, P. Anjukandi, B. Chul Kim and B. Ramachandra Bhat, *Chem. Eng. J.*, 2024, **500**, 156639.
22 R. Zeng, J. Xu, T. Liang, M. Li and D. Tang, *ACS Sens.*, 2023, **8**, 317–325.
23 H. Agarwal, S. Venkat Kumar and S. Rajeshkumar, *Resour.-Effic. Technol.*, 2017, **3**, 406–413.
24 D. S. Auld, *Biometals*, 2001, **14**, 271–313.
25 J. Singh, T. Dutta, K.-H. Kim, M. Rawat, P. Samddar and P. Kumar, *J. Nanobiotechnol.*, 2018, **16**, 84.
26 M. Bandeira, M. Giovanela, M. Roesch-Ely, D. M. Devine and J. Da Silva Crespo, *Sustainable Chem. Pharm.*, 2020, **15**, 100223.
27 E. G. Goh, X. Xu and P. G. McCormick, *Scr. Mater.*, 2014, **78–79**, 49–52.
28 S. Talam, S. R. Karumuri and N. Gunnam, *ISRN Nanotechnol.*, 2012, **2012**, 1–6.
29 X. Fang, K. Wang, D. Han, X. He, J. Wei, L. Zhao, M. U. Imam, Z. Ping, Y. Li, Y. Xu, J. Min and F. Wang, *BMC Med.*, 2016, **14**, 210.
30 G. C. Vidana Gamage, Y. Y. Lim and W. S. Choo, *Front. Plant Sci.*, 2021, **12**, 792303.
31 N. Wang, H.-Y. Tan, S. Li, Y. Xu, W. Guo and Y. Feng, *Oxid. Med. Cell. Longevity*, 2017, **2017**, 7478523.
32 B. Avinash, C. R. Ravikumar, N. Basavaraju, B. Abebe, T. N. Kumar, S. N. Manjula and H. C. A. Murthy, *Environ. Funct. Mater.*, 2023, **2**, 133–141.
33 G. S. Shivaganga, V. L. Ranganatha, T. L. Soundarya, G. Nagaraju, P. Parameswara, D. Ali and C. Mallikarjunaswamy, *Ionics*, 2024, **30**, 6667–6680.
34 A. M. Sayed, F. M. Salama, H. K. Galal and M. I. Said, *RSC Adv.*, 2025, **15**, 46890–46907.
35 Y. Li, Q. Pan, H. Shi, Y. Du, A. Yang and D.-P. Yang, *Microchem. J.*, 2025, **214**, 113957.
36 D. Feng, P. Huang, Y. Miao, A. Liang, X. Wang, B. Tang, H. Hou, M. Ren, S. Gao, L. Geng and A. Luo, *Sens. Actuators, B*, 2022, **368**, 132121.
37 H. Beitollahi, S. Tajik, F. Garkani Nejad and M. Safaei, *J. Mater. Chem. B*, 2020, **8**, 5826–5844.
38 G. C. Vidana Gamage, Y. Y. Lim and W. S. Choo, *Front. Plant Sci.*, 2021, **12**, 792303.
39 K. S. Mukunthan and S. Balaji, *Int. J. Green Nanotechnol.*, 2012, **4**, 71–79.
40 A. J. Love, V. V. Makarov, O. V. Sinitsyna, J. Shaw, I. V. Yaminsky, N. O. Kalinina and M. E. Taliansky, *Front. Plant Sci.*, 2015, **6**, 984.
41 A. Nobahar, J. D. Carlier, M. G. Miguel and M. C. Costa, *Biometals*, 2021, **34**, 761–793.
42 P. Pandey, Y. K. Shukla, J. P. Pandey, P. K. Singh and J. Kumar, *Biomass Convers. Biorefin.*, 2025, **15**, 17565–17576.
43 M.-A. Gatou, N. Lagopati, I.-A. Vagena, M. Gazouli and E. A. Pavlatou, *Nanomaterials*, 2022, **13**, 122.
44 M. Procek, T. Pustelny and A. Stolarczyk, *Nanomaterials*, 2016, **6**, 227.
45 R. Kripal, A. K. Gupta, R. K. Srivastava and S. K. Mishra, *Spectrochim. Acta, Part A*, 2011, **79**, 1605–1612.
46 S. Annathurai, S. Chidambaram, B. Baskaran and G. K. D. Prasanna Venkatesan, *J. Inorg. Organomet. Polym.*, 2019, **29**, 535–540.
47 N. Sedefoglu, *Optik*, 2023, **288**, 171217.
48 P. Rana, N. Murmu, S. K. Padhan and S. N. Sahu, *Spectrochim. Acta, Part A*, 2020, **237**, 118376.
49 D. Nipane, S. R. Thakare and N. T. Khati, *J. Catal.*, 2013, **2013**, 1–8.
50 M. Hjiri, S. Algessair, R. Dhahri, H. B. Albargi, N. Ben Mansour, A. A. Assadi and G. Neri, *RSC Adv.*, 2024, **14**, 5001–5011.
51 M. I. Alahmdi, S. Khasim, S. Vanaraj, C. Panneerselvam, M. A. A. Mahmoud, S. Mukhtar, M. A. Alsharif, N. S. Zidan, N. E. Abo-Dya and O. F. Aldosari, *J. Inorg. Organomet. Polym.*, 2022, **32**, 2146–2159.
52 S. Anantharaj, S. R. Ede, K. Karthick, S. Sam Sankar, K. Sangeetha, P. E. Karthik and S. Kundu, *Energy Environ. Sci.*, 2018, **11**, 744–771.
53 L. Rao, J. D. Rodney, Shivakumar, U. K. Dalimba, N. K. Udayashankar, B. C. Kim and B. R. Bhat, *Microchem. J.*, 2024, **204**, 111172.
54 L. Rao, J. D. Rodney, S. Sushmitha, F. J. Mascarenhas, M. P. Nayak, B. C. Kim and B. R. Bhat, *Microchem. J.*, 2025, **212**, 113371.
55 S. Sushmitha, S. Ray, L. Rao, M. P. Nayak, K. Carva and B. R. Bhat, *RSC Adv.*, 2025, 15, 34176–34190.
56 T. Sarkar, S. Kundu, G. Ghorai, P. K. Sahoo and A. Bhattacharjee, *Adv. Nat. Sci.: Nanosci. Nanotechnol.*, 2023, **14**, 035001.
57 S. Chakraborty, S. Sahoo, A. Bhagat and S. Dixit, *International Journal of Research -GRANTHAALAYAH*, 2017, **5**(10), 197–208.
58 L. Kaliraj, J. C. Ahn, E. J. Rupa, S. Abid, J. Lu and D. C. Yang, *J. Photochem. Photobiol., B*, 2019, **199**, 111588.
59 D. Mathew, B. Thomas, N. M. Sudheep and E. K. Radhakrishnan, *J. Photochem. Photobiol., A*, 2025, **468**, 116520.
60 S. S. Azahar, P. B. Raja, M. N. Mohamad Ibrahim, K. Awang, M. S. Zakeyuddin, T. S. Hamidon and M. H. Hussin, *J. Mol. Liq.*, 2024, **396**, 124056.
61 A. Devadoss, P. Sudhagar, C. Terashima, K. Nakata and A. Fujishima, *J. Photochem. Photobiol., C*, 2015, **24**, 43–63.
62 C. Zhu and X. Wang, *Nanomaterials*, 2025, **15**, 682.

© 2026 The Author(s). Published by the Royal Society of Chemistry